Sensors and Materials, Vol. 38, No. 4 (2026) 1975–1990
MYU Tokyo

S & M 4419

Geometry-modulated Modeling and System-level Simulation of a Thin-film Force Sensor Integrated with Pneumatic Artificial Muscles

Christian Rey M. Alison,[1] Loryliza D. Bulay-og,[2] and Aaron Raymond See[3*]

[1]Electrical Engineering Department, University of Science and Technology of Southern Philippines, Cagayan de Oro City 9000, Philippines
[2]Biomedical Engineering Department, University of Science and Technology of Southern Philippines, Alubijid Misamis Oriental 9018, Philippines
[3]Department of Electronic Engineering, National Chin-Yi University of Technology, Taiping District, Taichung City 411030, Taiwan

(Received December 15, 2025; accepted February 25, 2026)

Keywords: quadriceps, FlexiForce, pneumatic artificial muscle, mathematical modeling

The quadriceps muscle plays an essential role in locomotion and knee stability, yet conventional methods for muscle force estimation are often bulky, expensive, and invasive, limiting their suitability for continuous and scalable measurements. To address this limitation, we present a modeling and simulation framework that integrates a FlexiForce A502 thin-film sensor with a pneumatic artificial muscle (PAM) to emulate quadriceps-like force behavior. The proposed model establishes the relationship between internal chamber pressure and localized surface force, while the dynamic response of the thin-film sensor is characterized using a first-order differential equation. Experimental data were analyzed through curve fitting and parameter identification in MATLAB, yielding strong agreement between measured and simulated signals, with a coefficient of determination (R^2) of 0.934 and a root mean square error (*RMSE*) of 0.1493V, thereby validating the proposed modeling approach. A corresponding system-level simulation implemented in Simulink demonstrated that PAM input pressures ranging from 120 to 600 kPa can generate localized patch forces of up to 450 N. These results verify the feasibility of thin-film sensors for real-time muscle-like force estimation and highlight their potential applications in biomechanics, rehabilitation, and soft robotic systems.

1. Introduction

The quadriceps muscle group is one of the most powerful in the human musculoskeletal system and is essential for knee extension and lower-limb stabilization.[1–3] Clinical evidence shows that reduced quadriceps strength compromises these functions, leading to mobility impairments and an increased risk of knee pathologies such as osteoarthritis and patellofemoral pain syndrome.[4–6] Globally, osteoarthritis affects over 240 million people, with quadriceps weakness identified as a major contributing factor.[7,8] In the context of the Philippines, nearly

*Corresponding author: e-mail: aaronsee@gm.ncut.edu.tw
https://doi.org/10.18494/SAM6120

ISSN 0914-4935
https://myukk.org/

20% of adults aged 60 and above suffer from symptomatic knee osteoarthritis, where quadriceps weakness accelerates functional decline.[9,10] Despite its clinical significance, many individuals remain unaware of their muscle weakness until mobility limitations and pain manifest.[11–13] Accurate monitoring of quadriceps muscle force is therefore critical for rehabilitation, performance evaluation, and early detection of functional decline.[14–17]

Traditional methods such as isokinetic dynamometry provide reliable torque measurements but are bulky, costly, and limited to laboratory environments.[18–20] Portable alternatives like handheld dynamometers improve accessibility but remain prone to examiner bias and reduced reliability at higher force outputs.[21–23] These limitations have driven the development of flexible thin-film sensing technologies capable of real-time, localized force detection in wearable or embedded configurations.[24,25]

Among these, piezoresistive thin-film sensors, such as the FlexiForce series, have gained attention for use in biomechanical monitoring owing to their compact size, high sensitivity, and ability to conform to curved surfaces.[26–28] Xu *et al.* highlighted their potential in wearable force arrays,[29] while Sun *et al.* and Zhang *et al.* demonstrated structural and multidirectional improvements for specific applications.[30,31] Similarly, Esposito *et al.* and others developed an Force-Sensitive Resistor (FSR)-based sensor correlated with electromyography (EMG) signals ($r > 0.9$), confirming their suitability for muscle activity monitoring.[32–34] However, most of these studies remain confined to static testing or surface-level measurements, lacking integration with systems that replicate physiological muscle dynamics.

To address this research gap, in this study, we integrate a thin-film force sensor with a pneumatic artificial muscle (PAM) to emulate quadriceps-like contractions and evaluate sensor behavior under dynamic loading. PAMs are known for their biomimetic motion and nonlinear force–pressure–length relationship,[35–41] making them suitable for simulating physiological muscle dynamics. A pressure-geometry-coupled thin-film model was developed and implemented in MATLAB/Simulink to simulate real-time biomechanical force estimation. The model effectively captures both static and dynamic responses, providing a computational basis for accurate and scalable muscle force sensing in rehabilitation, prosthetics, and assistive robotics.

2. Materials and Methods

2.1 System overview and setup

In the present work, a thin-film force sensor is employed to measure the localized surface force generated during PAM actuation, providing a compact and flexible alternative to conventional dynamometric setups. This configuration enables direct coupling between pneumatic pressure input and the electrical response of the sensor, forming the foundation for the modeling and simulation framework.

To characterize and simulate the dynamic behavior of a single PAM under varying pressure conditions, we used a hardware-referenced schematic and a computational model. The schematic in Fig. 1(a) defines the physical interfaces and variables used in the simulation. PAM1 denotes

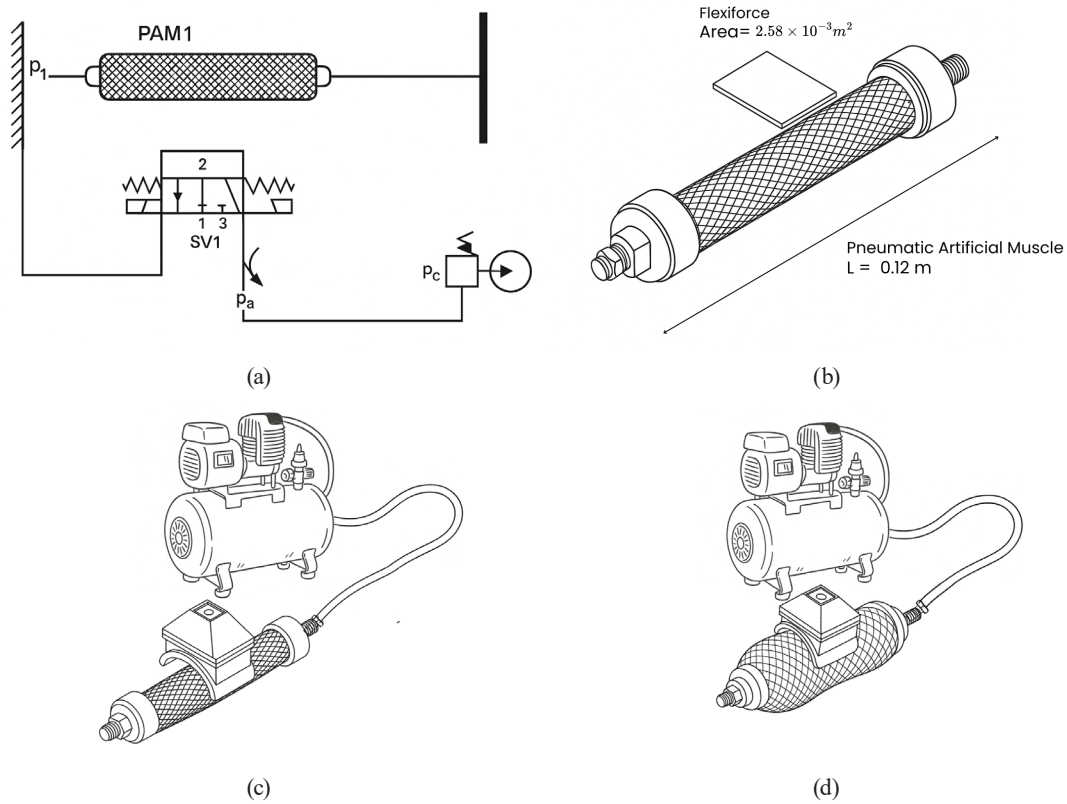

Fig. 1. (a) PAM-based actuator and pneumatic circuit used to ground the simulation and modeling, (b) initial arrangement of the PAM and thin-film element, (c) FlexiForce-integrated PAM setup connected to the air compressor in the deflated state, and (d) inflated PAM condition with air-compressor supply, showing radial expansion and axial contraction producing measurable surface pressure.

the actuator, SV1 is a 3/2-way solenoid valve that switches the chamber between supply and exhaust, P_a is the air-supply line to SV1, P_1 is the PAM chamber pressure downstream of SV1, and P_c is the compressor line pressure. During actuation, energizing SV1 connects the supply to the chamber so P_1 rises and the muscle inflates, and de-energizing vents the chamber so P_1 falls and the muscle deflates. This configuration served as the basis for the simulation blocks and the mathematical derivation of the patch-force model.

2.2 Materials and specifications

Two primary components were used in this study, namely, a thin-film force sensor and a PAM, as shown in Fig. 2. The sensing element used in this study was the FlexiForce A502 [Fig. 2(a)], a piezoresistive thin-film sensor designed for distributed surface pressure measurements. It features a square active region measuring 50.8 × 50.8 mm^2, corresponding to a nominal sensing area of 2.58 × 10^{-3} m^2. This can measure forces from 222 to 44448 N and has a typical linearity of ±3% of full-scale force capacity. Owing to its thin, flexible polyester substrate, the sensor conforms well to curved surfaces such as the outer wall of the PAM, ensuring stable contact during actuation. Figure 2(b) shows the actuator used, Festo DMSP-40-120-RM-CM, a

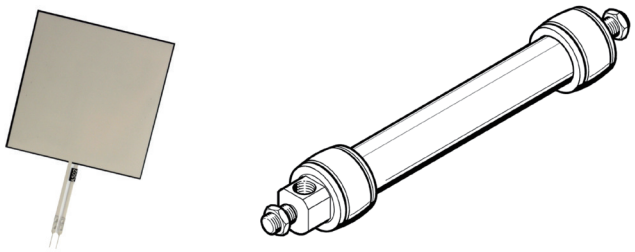

(a) (b)

Fig. 2. (Color online) (a) FlexiForce A502 thin-film force sensor and (b) Festo DMSP-40-120-RM-CM PAM.

McKibben-type PAM designed to emulate biological muscle contraction. The PAM consists of a flexible elastomer tube encased in a fiber-reinforced sleeve with metal end fittings for pneumatic connection. It has a nominal length of 120 mm, an outer diameter of 40 mm, and operates effectively within an input pressure range of 0–600 kPa. The specifications of the two components are given in Tables 1 and 2, respectively.

3. Mathematical Modeling and System Simulation

3.1 Thin-film patch-force mathematical modeling derivation

Building upon the classical Chou–Hannaford formulation,[37] which relates the actuator's axial force to its internal pressure and geometric configuration, the present work adapts this relationship to describe the localized surface force acting on the thin-film sensing region. When the PAM is inflated, the internal pressure generates a distributed normal stress $\sigma_n(x, t)$ on the inner bladder wall, where x denotes the spatial coordinate on the surface and t denotes time.

As the wall expands radially, this distributed stress is conveyed through the elastic bladder and adhesive interface to the external surface where the thin-film sensor is mounted. Assuming that the patch area is small relative to the total muscle surface and that local curvature remains approximately constant, the total patch force F_{patch} can be expressed as the surface integral of this wall traction over the sensor's effective active area A_{eff}:

$$F_{patch}(t) = \int_{A_{eff}} \sigma_n(x,t)dA\,. \tag{1}$$

Here, $\sigma_n(x, t)$ represents the distributed pressure intensity and dA is the infinitesimal surface element. Their product $\sigma_n dA$ yields a differential force element; integration over A_{eff} provides the resultant total force acting on the patch.

Under the reasonable assumption that the stress field is nearly uniform across the small sensing area, the integral simplifies to

$$F_{patch} = A_{eff}\sigma_n(t)\,. \tag{2}$$

Here, the effective active area A_{eff} depends on the physical footprint of the sensor and the mechanical coupling efficiency between the bladder and the patch. It can be written as

Table 1
Performance characteristics of the FlexiForce A502 sensor.

Parameter	Typical Performance
Linearity (error)	< ±3% of full scale
Repeatability	< ±2.5%
Hysteresis	< 4.5% of full scale
Drift	< 5% per logarithmic time scale

Table 2
Specifications of the Festo DMSP-40-120-RM-CM pneumatic muscle.

Feature	Value
Nominal size (diameter)	40 mm
Nominal length	120 mm
Maximum contraction	25% of nominal length
Maximum initial tension	5% of nominal length
Maximum working load (freely suspended)	250 kg
Theoretical muscle force at 0.6 MPa (6 bar, 87 psi)	6000 N
Operating pressure	600 kPa

$$A_{eff} = \eta A_g , \tag{3}$$

where $A_g = wh$ is the geometric area of a rectangle and $0 < \eta \leq 1$ accounts for contact-efficiency losses arising from nonuniform adhesion, edge effects, or slight detachment.

Now, to represent how this normal stress varies with the internal chamber pressure, the local traction $\sigma_n(t)$ is expressed as a low-order polynomial in $p(t)$ with an additional rate-dependent term $p'(t)$ that captures transient viscoelastic effects of the wall–sensor assembly:

$$\sigma_n(t) = c_0 + c_1 p(t) + c_2 p^2(t) + c_3 p'(t) , \tag{4}$$

where $p(t)$ is the instantaneous chamber pressure and $p'(t)$ is its time derivative. Substituting Eq. (4) into the stress–area relation of Eq. (2) gives the thin-film patch-force equation

$$F_{patch}(t) = A_{eff}[c_0 + c_1 p(t) + c_2 p^2(t) + c_3 p'(t)] , \tag{5}$$

where c_0, c_1, c_2, and c_3 are empirical pressure–stress mapping coefficients identified through curve fitting. Specifically, c_0 represents the baseline normal stress contribution under near-zero pressure conditions, reflecting residual contact stress and preload effects at the PAM–sensor interface. The coefficients c_1 and c_2 characterize the first- and second-order pressure-dependent contributions to the local normal stress, capturing the nonlinear transmission of chamber pressure through the elastic PAM membrane and compliant sensor interface. The rate-dependent coefficient c_3 scales the pressure derivative term $p'(t)$ and accounts for transient viscoelastic effects associated with the time-dependent deformation of the PAM bladder and the polymer substrate of the thin-film sensor under dynamic loading. The constant and polynomial pressure terms describe the static response of the patch, whereas the derivative term captures the dynamic

rate-dependent effects arising from the viscoelastic properties of the PAM membrane and the sensor substrate. Furthermore, the inclusion of the pressure derivative term $p(t)$ allows the model to capture rate-dependent effects associated with the transient viscoelastic behavior of both the PAM membrane and the polymer-based thin-film sensor. This reduced-order representation also implicitly accounts for bounded hysteresis and short-term drift effects under cyclic loading conditions, consistent with the sensor characteristics reported in Table 1.

To account for the influence of actuator geometry on the local pressure distribution, the linear pressure term in Eq. (5) can be further expressed as a function of a dimensionless geometry modulation factor $g(t)$. The inclusion of this term follows the Chou–Hannaford observation[37] that axial force varies with the braid angle according to the factor $(3\cos^2\theta - 1)$. By introducing an affine modulation of the pressure coefficient, the patch-force equation becomes

$$F_{patch}(t) = A_{eff}\left[c_0 + (k_0 + k_1 g(t))\,p(t) + c_2 p^2(t) + c_3 p'(t)\right]. \tag{6}$$

In Eq. (6), k_0 and k_1 are dimensionless geometry-dependent gains that modulate the linear pressure term according to the actuator's instantaneous configuration. The parameter k_0 corresponds to the nominal pressure-to-force gain under the reference configuration of the PAM, while k_1 quantifies how this gain varies with the braid angle through the modulation factor $g(t)$. Both coefficients originate from the geometric scaling of the Chou–Hannaford axial-force relation, where the effective area projection is proportional to $(\pi D^2/4)(3\cos^2\theta - 1)$. In the present formulation, the global cross-sectional area term is already incorporated in A_{eff}; thus, k_0 and k_1 express only the relative geometric influence and remain dimensionless. Their empirical form can be written as

$$k_0 = \alpha_0 \frac{A_{Chou}}{A_{eff}} \quad k_1 = \alpha_1 \frac{A_{Chou}}{A_{eff}}, \tag{7}$$

where $A_{Chou} = (\pi D^2/4)$ is the PAM's nominal cross-sectional area and α_0, α_1 are empirical scaling constants determined through curve fitting. Because both parameters are ratios of areas, k_0 and k_1 are dimensionless and typically fall within the ranges 0.5–1.2 and 0.1–0.5, respectively, depending on actuator geometry and wall stiffness.

To describe the effect of braid angle variation during contraction, the geometry modulation factor $g(t)$ is defined as a function of the instantaneous actuator length $L(t)$ and braid length b:

$$g(t) = 3\left(\frac{L(t)}{b}\right)^2 - 1. \tag{8}$$

Substituting Eq. (7) into Eq. (6) yields the pressure-geometry-coupled form of the patch-force model:

$$F_{patch}(t) = A_{eff}[c_0 + (k_0 + k_1(3(L/b)^2 - 1))p(t) + c_2 p^2(t) + c_3 p'(t)]. \quad (9)$$

Equation (9) represents the complete pressure–geometry–force relationship of the thin-film sensing system, linking the chamber pressure, actuator length, and resulting patch force. This formulation consolidates the effects of pressure nonlinearity, dynamic rate dependence, and geometric modulation within a single model, providing the mathematical foundation for parameter identification and system simulation.

Building upon this formulation, the relationships expressed in Eqs. (1)–(9) collectively define the governing interaction between pneumatic pressure, actuator geometry, and the localized surface traction acting on the thin-film sensor. This coupled representation captures both static and dynamic characteristics of the sensing process, including the combined effects of membrane viscoelasticity, pressure nonlinearity, and geometric modulation. The resulting mathematical model provides a unified framework that can be directly implemented in MATLAB/Simulink for parameter estimation and dynamic analysis.

To facilitate interpretation and ensure dimensional consistency, all parameters and variables introduced in Eqs. (1)–(9) are summarized in Table 3, which lists each symbol, its description, unit, and functional role within the model.

3.2 Sensor dynamic modeling

The FlexiForce sensor behaves as a force-dependent resistive element, whose resistance decreases approximately linearly with increasing load near its operating range. When connected in a voltage divider or transimpedance configuration, the resulting circuit can be modeled by a single-pole low-pass filter with time constant τ_s and static gain κ_s. In the Laplace domain, the input–output relationship between the patch force and the measured voltage is

Table 3
Parameters and variables used in the thin-film patch-force model.

Symbol	Description	Unit	Role in model
F_{patch}	Patch force	N	Resultant force transmitted to the thin-film sensor
$p(t)$	Chamber pressure	Pa	Primary excitation input
$p'(t)$	Pressure rate	Pa s^{-1}	Change in pressure
$\sigma_n(t)$	Normal stress on patch surface	Pa	Distributed traction acting on sensing region
A_{eff}	Effective sensing area	m^2	Converts surface stress to resultant patch force
$L(t)$	Instantaneous actuator length	m	Defines current PAM configuration
b	Braid length	m	Constant geometric reference
c_0, c_1, c_2, c_3	Polynomial coefficients	Pa, —, 1/Pa, s	Define static and dynamic pressure–stress mapping
k_0, k_1	Geometry-dependent gains	—	Modulate pressure–geometry coupling
$g(t)$	Geometry modulation factor	—	Represents braid-angle variation with contraction
η	Contact-efficiency factor	—	Accounts for imperfect adhesion between patch and bladder wall

$$\frac{V_s(s)}{F_{patch}(s)} = \frac{\kappa_s}{\tau_s s + 1}. \tag{10}$$

Taking the inverse Laplace transform of Eq. (10) provides the corresponding time-domain equation governing the transient and steady-state voltage response:

$$\tau_s V_s'(t) + V_s(t) = k_s F_{patch}(t) + b_s. \tag{11}$$

Equation (11) describes the sensor's dynamic response and links the applied patch force to the measured voltage through a first-order differential model. Here, τ_s denotes the sensor time constant, κ_s represents the sensitivity gain, $V_s'(t)$ is the time derivative of the sensor voltage, and b_s corresponds to the baseline offset under unloaded conditions. The term $V_s(t)$ denotes the instantaneous model-predicted voltage generated by the applied patch force $F_{patch}(t)$ obtained from Eq. (9). As a result, Eq. (11) defines the mathematical link between the mechanical and electrical domains of the thin-film sensing system, unifying force dynamics, circuit response, and baseline offset into a model that reproduces the observed voltage behavior. For clarity, the parameters and variables used are summarized in Table 4.

3.3 Thin-film patch-force sensing system simulation

Following the curve fitting verification for Eqs. (9) and (11), the identified parameters are integrated into a system-level simulation to evaluate the dynamic performance of the thin-film sensing model within the PAM actuation framework. The goal is to verify the model's ability to reproduce the pressure–force–voltage response. The simulation is implemented in MATLAB/Simulink, where the mechanical and electrical formulations in Eqs. (8) and (10) are combined into a unified framework, as shown in Fig. 3. The patch-force equation obtained from curve fitting is embedded in a MATLAB function block (Patch-force Block) and coupled with the PAM pneumatic subsystem, which includes valve actuation, bias and clamp constraints, and unit conversion elements governing chamber pressurization.

In Fig. 3, on the left, the striped blocks represent the external control signal inputs, U_i and U_o, which define the activation of the inlet and outlet valves. These inputs are processed through comparator blocks that check whether the signals exceed a threshold value, thereby determining

Table 4
Parameters and variables of the sensor-dynamic model.

Symbol	Description	Unit	Role in Model
F_{patch}	Input patch-force Eq. (13)	N	Mechanical input to the sensor model
$V_s(t)$	Sensor output voltage	V	Output at zero applied force
$V_s'(t)$	Time derivative of sensor voltage	V	Captures transient rate of voltage change
τ_s	Sensor/circuit time constant	s	Defines response speed of the sensor–circuit system
κ_s	Sensitivity gain	V N^{-1}	Converts mechanical force to voltage amplitude
b_s	Baseline offset voltage	V	Output at zero applied force

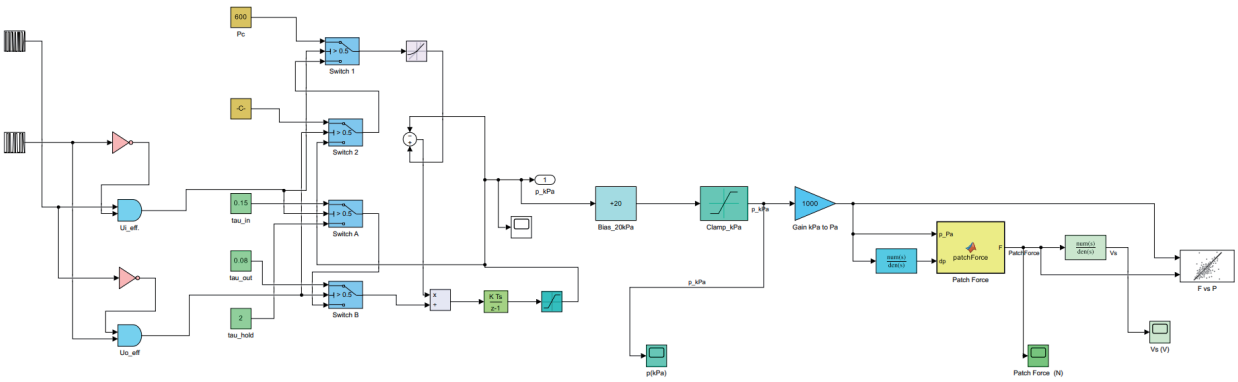

Fig. 3. (Color online) Schematic of the overall simulation framework, emphasizing the sequential interaction between pneumatic pressure, actuator geometry, patch-force generation, and thin-film voltage response.

the ON/OFF state of the valves. The resulting outputs are passed through logic blocks labeled $U_{i,eff}$ and $U_{o,eff}$, which generate the effective valve actuation commands used in the pneumatic circuit. The valve dynamics are modeled using constant sources for the compressed air supply pressure P_c = 600 kPa and P_a = 101.325 kPa.

Time constants (T_{in}, T_{out}, T_{hold}) control the inlet, outlet, and holding phases of valve operation, while switching elements route the airflow accordingly. A flow resistance block accounts for losses during valve transitions. These signals are combined at the summation block to compute the net airflow into the PAM chamber. A discrete-time integrator D_t accumulates this input to estimate the chamber pressure over time, while a saturation S_t block ensures that pressure values remain within realistic operating limits. The resulting chamber pressure, expressed in kilopascals, is first offset by a 20 kPa bias, clamped to valid bounds, and then converted from kPa to Pa through a gain block. This pressure signal serves as the input to the patch-force block, which contains the mathematical model derived from curve fitting. Inside this block, the localized surface force acting on the FlexiForce thin-film sensor is computed as a function of chamber pressure and its rate of change.

4. Results and Discussion

4.1 Parameter identification through curve fitting

To determine the unknown coefficients of the mechanical and electrical subsystems, the parameters in Eqs. (9) and (11) were identified using a nonlinear least-squares curve-fitting approach in MATLAB. The dataset used for identification consisted of the recorded chamber pressure $p(t)$, its time derivative $p'(t)$, and the corresponding thin-film sensor voltage $V_s(t)$. The effective patch area A_{eff} and braid length b were held constant on the basis of prior geometric calibration, while the polynomial coefficients (c_0, c_1, c_2, c_3), geometry-dependent gains (k_0, k_1), and sensor-dynamic constants (τ_s, κ_s, b_s) were treated as unknowns. The optimization routine minimized the root mean square error ($RMSE$) between the measured and simulated voltages,

ensuring both amplitude and phase consistency across loading cycles. Each iteration evaluated the voltage predicted by the combined pressure–geometry–force–voltage pathway,

$$\tau_s V_s'(t) + V_s(t) = k_s A_{eff}[c_0 + (k_0 + k_1 g(t))p(t) + c_2 p^2(t) + c_3 p'(t)] + b_s . \quad (12)$$

The derived model in Eq. (12) was fitted to the experimental data to estimate the unknown parameters governing the coupled pressure–geometry–voltage behavior of the thin-film sensor, incorporating both the pressure–geometry formulation [Eq. (9)] and the first-order voltage dynamics [Eq. (10)].

The curve-fitting process yielded a reconstructed voltage response that closely matched the measured signal, as illustrated in Fig. 4. The fitting results are summarized in Figs. 4(a)–4(d), which present the measured and simulated voltage responses, the input chamber pressure and geometry-dependent modulation term $g(t) = 3(L/b)^2 - 1$, the reconstructed patch force, and the resulting pressure–force relationship, respectively. During the initial unactuated phase (0–2 s), both pressure and voltage remain near baseline levels. As the chamber inflates (2–6 s), the voltage response follows the pressure input with a short delay consistent with the first-order sensor dynamics. Figure 4(a) shows the close agreement between the measured and simulated voltages, yielding $RMSE$ = 0.1493 V and R^2 = 0.934, confirming that the model accurately captures the dominant pressure–force–voltage dynamics. Figure 4(c) shows that the reconstructed patch force follows the periodic pressure input with minimal distortion and a

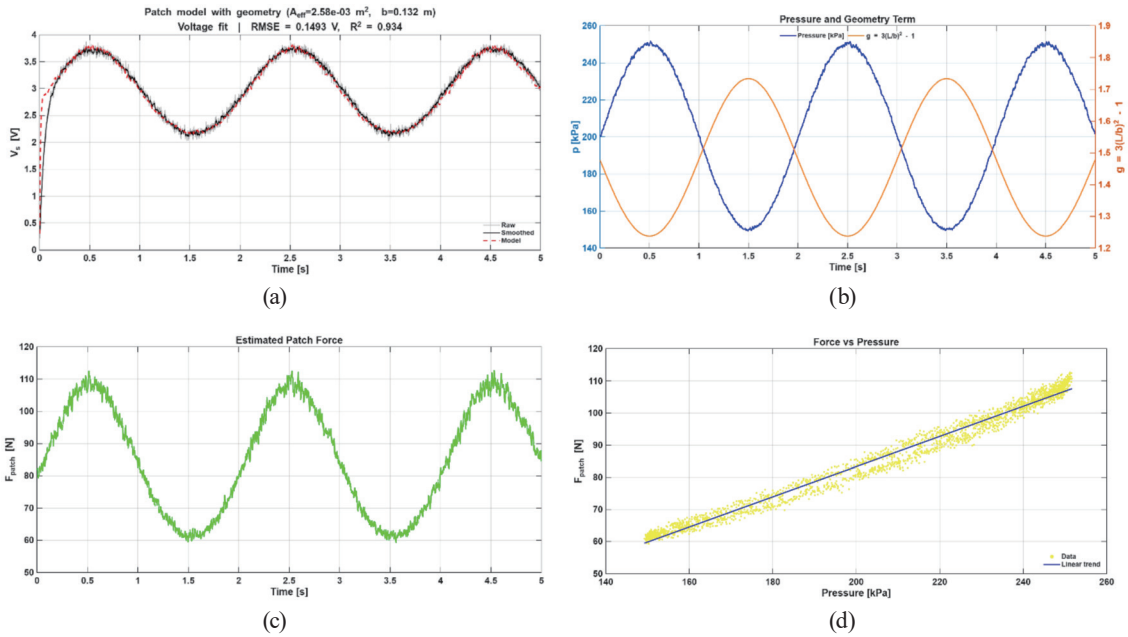

Fig. 4. (Color online) Model fitting results for the thin-film patch sensor based on the pressure–geometry coupled form [Eq. (8)] and the sensor's dynamic response [Eq. (10)]: (a) measured and simulated sensor voltages showing good agreement with the model fit ($RMSE$ = 0.1493 V, R^2 = 0.934); (b) pressure waveform and geometry term $g = 3(L/b)^2 - 1$ during alternating inflation–deflation cycles; (c) reconstructed patch-force response derived from the fitted parameters; and (d) quasi-static pressure–force relationship with linear regression fit confirming the proportionality between pneumatic pressure and generated patch force.

peak-to-peak range of approximately 60–110 N. Finally, Fig. 4(d) shows a strong linear correlation between chamber pressure and estimated patch force, validating the pressure–geometry coupling described in Eq. (9).

The resulting optimal coefficients, summarized in Table 5, represent the parameter set that yields the highest coefficient of determination R^2 and the lowest *RMSE* between the model output and measured voltage. These parameters were subsequently used for dynamic simulation and validation.

4.2 Integration of the patch-force model and system simulation

Following the successful identification and validation of the unknown coefficients presented in Sect. 4.1, we integrate the geometry-modulated thin-film sensing model into the PAM framework to evaluate its dynamic performance under cyclic actuation. The results of the system-level simulation in Fig. 3 provide further insight into how localized surface forces evolve in response to time-varying chamber pressures, thereby verifying the applicability of the identified parameters within a complete actuator system. In Fig. 5, the temporal evolution of the PAM during successive inflation–deflation cycles is illustrated. As shown in Fig. 5(a), the internal chamber pressure oscillates between approximately 120 and 600 kPa with intervals of 5 to 6 s per cycle, representing the valve-controlled charging and discharging phases. The steep pressure rises between 2–4 and 8–10 s correspond to rapid chamber filling, while the sudden drops mark the controlled release phase. These variations accurately reproduce the dynamic characteristics of pneumatic actuation governed by valve-switching logic. The corresponding patch-force response in Fig. 5(b) demonstrates how the internal pressure variations are effectively transduced into localized surface forces through the FlexiForce A502 thin-film sensor.

The simulated patch force follows the same periodic pattern as the chamber pressure, with peak forces reaching approximately 450 N during each inflation sequence and returning close to baseline upon deflation. The reported patch force of approximately 450 N does not represent a concentrated point load applied directly to the FlexiForce A502 sensor. Rather, it corresponds to a reconstructed, distributed surface force generated by the PAM and transmitted through the compliant PAM–sensor contact interface. In practice, thin-film force sensors such as FlexiForce A502 are commonly operated beyond their nominal test range through appropriate circuit

Table 5
Values of unknown parameters for geometry-modulated patch model.

Parameter	Value
c_0	-9.083 N/m^2
c_2	3.254×10^{-6} 1/Pa
c_3	-2.158×10^{-3} s/Pa
k_0	-1.435
k_1	6.377×10^{-1}
τ_s	3.321×10^{-2} s
κ_s	8.325×10^{-3} V/N
b_s	1.470×10^{-1} V

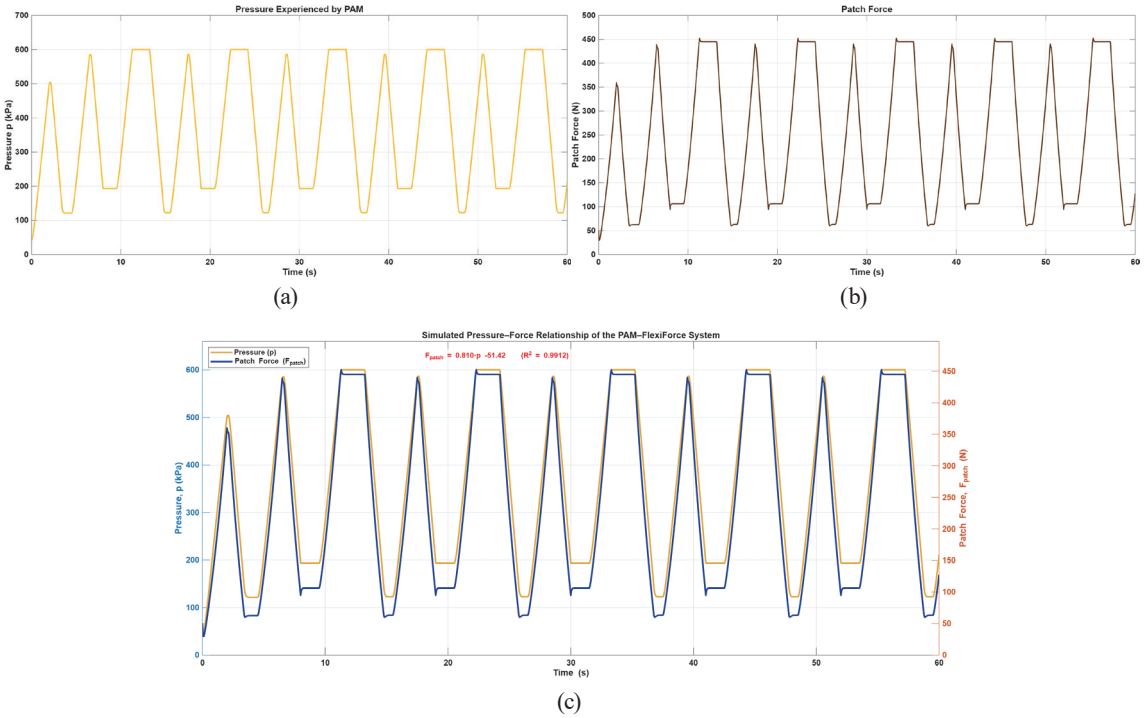

Fig. 5. (Color online) Simulated dynamic response of the PAM integrated with the geometry-modulated thin-film force sensing model: (a) internal pressure profile of the PAM under cyclic inflation–deflation actuation; (b) simulated patch-force response measured by the FlexiForce A502 thin-film sensor mounted on the PAM surface; and (c) combined pressure–force waveform illustrating the synchronization between chamber pressure dynamics and generated patch force during repeated actuation cycles.

configuration and calibration, as indicated by the manufacturer. In the present setup, the applied load is spatially distributed over the effective sensor contact area and the sensor output remains within its linear operating regime. As a result, no saturation, damage, or severe nonlinearity is observed, and the reported patch force reflects a model-based reconstruction of the global surface force rather than a direct exceedance of the nominal point-load rating. This consistent temporal alignment validates the pressure–force coupling derived from the fitted model coefficients. Meanwhile, Fig. 5(c) presents the combined pressure–force waveform, highlighting a strong linear relationship between the two parameters, which is expressed as

$$F_{patch} = 0.810\,p - 51.42\,, \tag{13}$$

with a coefficient of determination $R^2 = 0.9912$. While the system-level simulation confirms a strong linear pressure–force relationship, additional insight can be obtained by revisiting the experimental pressure–force behavior presented earlier in Fig. 4(d). It is worth noting that the experimental pressure–force data in Fig. 4(d) exhibit a narrow loop between the inflation and deflation phases, which reflects the inherent hysteresis behavior of PAM. This hysteresis primarily arises from the viscoelastic properties of the elastomeric bladder, friction within the braided sleeve, and transient airflow dynamics during pressurization and exhaust. Although this

effect results in slightly different force trajectories for increasing and decreasing pressure, the deviation remains small within the tested operating range.

As evidenced by the high coefficient of determination $R^2 = 0.9912$, the overall pressure–force relationship remains predominantly linear. Consequently, the observed hysteresis is expected to have only a minor impact on practical force estimation and control, particularly in quasi-static or feedback-regulated applications where such nonlinearities can be effectively compensated. The near unity R^2 value confirms that the modeled patch force accurately captures the proportionality between chamber pressure and generated surface force.

The minimal deviation between the simulated and fitted responses further demonstrates the robustness of the geometry-modulated model in reproducing both the magnitude and timing of dynamic actuation. A minor phase shift between the two signals is observed, attributed to the viscoelastic response of the PAM membrane and the polymer substrate of the thin-film sensor, which introduces a time-dependent lag. This behavior is consistent with the bounded hysteresis, short-term drift, and rate-dependent characteristics of thin-film force sensors operating under cyclic loading conditions, as summarized in Table 1. The results confirm that the integrated model reliably reproduces the pneumatic–mechanical conversion and localized force transduction of the PAM system, reinforcing its suitability for real-time biomechanical and soft-robotic applications where the accurate monitoring of dynamic muscle-like forces is essential.

5. Conclusions

In this study, we successfully developed and validated a mathematical modeling and system-level simulation framework that links the PAM actuation dynamics with the surface forces detected by a thin-film FlexiForce A502 sensor. The mathematical model, obtained via nonlinear curve fitting, accurately reproduced experimental sensor responses ($R^2 = 0.934$, $RMSE = 0.1493$ V). In the integrated system-level simulation, the pressure–force coupling exhibited a strong linear relationship, $F_{patch} = 0.810p - 51.42$ with $R^2 = 0.9912$, and minimal deviation between simulated and fitted responses. The simulation further verified that chamber pressures from 120 to 600 kPa generated patch forces up to 450 N, with synchronized oscillations between pressure and patch-force signals and only a minor phase delay. These results confirm a reliable pneumatic–mechanical–electrical interaction and provide a practical, scalable basis for estimating quadriceps muscle forces through biomimetic sensing, supporting future applications of the PAM system in prosthetics, rehabilitation, and assistive robotic systems.

Acknowledgments

This work was supported in part by the National Science and Technology Council of Taiwan under grant number NSTC 114-2221-E-167 -007 -MY2.

References

1 Y. Ito, T. Aoki, T. Sato, K. Oishi, and K. Ishii: BMJ Open Sport Exerc. Med. **6** (2020) e000753. https://doi.org/10.1136/bmjsem-2020-000753
2 F. Kukić, V. Mrdaković, A. Stanković, and D. Ilić: Biology **11** (2022) 1490. https://doi.org/10.3390/biology11101490
3 A. Buchmann, B. Kiss, A. Badri-Spröwitz, and D. Renjewski: Sci. Rep. **15** (2025) 2249. https://doi.org/10.1038/s41598-025-86147-z
4 G. Kitamura, M. Nankaku, T. Yuri, T. Kawano, S. Kuriyama, S. Nakamura, K. Nishitani, R. Ikeguchi, and S. Matsuda: Clin. Nutr. ESPEN **64** (2024) 418. https://doi.org/10.1016/j.clnesp.2024.10.160
5 B. E. Øiestad, C. B. Juhl, I. Eitzen, and J. B. Thorlund: Osteoarthritis Cartilage **23** (2015) 171. https://doi.org/10.1016/j.joca.2014.10.008
6 K. Nishino, H. Koga, Y. Koga, M. Tanaka, A. Nawata, K. Endoh, M. Arakawa, and G. Omori: Clin. Biomech. **84** (2021) 105325. https://doi.org/10.1016/j.clinbiomech.2021.105325
7 World Health Organization: "Musculoskeletal health" https://www.who.int/news-room/fact-sheets/detail/musculoskeletal-conditions (accessed August 26, 2025).
8 World Health Organization: "Osteoarthritis" https://www.who.int/news-room/fact-sheets/detail/osteoarthritis (accessed October 9, 2025).
9 P. Francisco, L. Nicodemus, S. Laviña, and E. G. Penserga: Osteoarthritis Cartilage **26** (2018) S265. https://doi.org/10.1016/j.joca.2018.02.540
10 G. Z. Racaza, E. O. Salido, and E. G. Penserga: Int. J. Rheum. Dis. **15** (2012) 399. https://doi.org/10.1111/j.1756-185X.2012.01758.x
11 N. A. Glass, J. C. Torner, L. A. Frey Law, K. Wang, T. Yang, M. C. Nevitt, D. T. Felson, C. E. Lewis, and N. A. Segal: Osteoarthritis Cartilage **21** (2013) 1154. https://doi.org/10.1016/j.joca.2013.05.016
12 T. J. Zhai, F. Y. Jiang, Y. P. Chen, J. Wang, and W. Feng: Front. Med. **11** (2024) 1433070. https://doi.org/10.3389/fmed.2024.1433070
13 D. A. Sherman, T. Neogi, S. Hornsby, D. Felson, M. Lavalley, J. J. Stefanik, and OAI Investigators: ACR Open Rheumatol. **7** (2025) e70067. https://doi.org/10.1002/acr2.70067
14 A. Scano, R. Re, A. Tomba, O. Amata, I. Pirovano, C. Brambilla, D. Contini, L. Spinelli, C. Amendola, A. V. Caserta, R. Cubeddu, L. Panella, and A. Torricelli: Appl. Sci. **13** (2023) 6855. https://doi.org/10.3390/app13116855
15 K. B. MacDougall, S. J. Aboodarda, P. H. Westergard, and B. R. MacIntosh: Eur. J. Sport Sci. **24** (2024) 1328. https://doi.org/10.1002/ejsc.12181.
16 W. Welling, J. Paalman, R. Speerstra, A. Van Houten, and R. Hoogeslag: J. Orthop. **59** (2025) 128. https://doi.org/10.1016/j.jor.2024.11.005
17 M. F. Güven, M. Özer, M. K. Özşahin, G. U. Değer, İ. Adaletli, O. A. Kargin, G. Kaynak, and H. Botanlıoğlu: Arch. Orthop. Trauma Surg. **144** (2024) 4839. https://doi.org/10.1007/s00402-024-05570-5
18 S. Ahmadi and M. C. Uchida: Hum. Mov. **22** (2021) 1. https://doi.org/10.5114/hm.2021.100319
19 Z. Dvir and S. Müller: J. Strength Cond. Res. **34** (2020) 587. https://doi.org/10.1519/JSC.0000000000002982
20 Hawkin Dynamics: "Fixed vs Unfixed Dynamometry Explained" https://www.hawkindynamics.com/blog/fixed-vs-unfixed-dynamometry (accessed October 9, 2025).
21 J. Marušič, G. Marković, and N. Šarabon: Appl. Sci. **11** (2021) 3391. https://doi.org/10.3390/app11083391
22 M. A. C. Garcia, D. S. Fonseca, and V. H. Souza: Braz. J. Phys. Ther. **25** (2021) 231. https://doi.org/10.1016/j.bjpt.2020.09.003
23 F. Aerts, H. Sheets, C. Anderson, N. Bussie, R. Hoskins, A. Maninga, and E. Novak: Int. J. Sports Phys. Ther. **20** (2025) 253. https://doi.org/10.26603/001c.128286
24 T.-D. Nguyen and J. S. Lee: Sensors **22** (2021) 50. https://doi.org/10.3390/s22010050
25 N. M. Vidyanag, J. Grant, J. Dahl, J. Yoon, and M. Cakmak: ACS Appl. Mater. Interfaces **17** (2025) 36148. https://doi.org/10.1021/acsami.5c03350
26 N.-I. Kim, J. M. Lee, M. Moradnia, J. Chen, S. Pouladi, M. Yarali, J. Y. Kim, M.-K. Kwon, T. R. Lee, and J.-H. Ryou: Soft Sci. **5** (2025). https://doi.org/10.20517/ss.2025.33
27 L. Zhen, M. Cui, X. Bai, J. Jiang, X. Ma, M. Wang, J. Liu, and B. Yang: Nano Energy **131** (2024) 110188. https://doi.org/10.1016/j.nanoen.2024.110188
28 N. Luo: Flexible Piezoresistive Sensors for Biomedical Applications (The Chinese University of Hong Kong, Hong Kong, 2017) also available at https://www.webofscience.com/wos/alldb/full-record/PQDT:67032721 (accessed October 9, 2025).

29 S. Xu, Z. Xu, D. Li, T. Cui, X. Li, Y. Yang, H. Liu, and T. Ren: Polymers **15** (2023) 2699. https://doi.org/10.3390/polym15122699
30 R. Sun, P. Xiao, L. Sun, D. Guo, and Y. Wang: Sensors **24** (2024) 8114. https://doi.org/10.3390/s24248114
31 J. Zhang, X. Hou, S. Qian, J. Huo, M. Yuan, Z. Duan, X. Song, H. Wu, S. Shi, W. Geng, J. Mu, J. He, and X. Chou: Microsyst. Nanoeng. **10** (2024) 64. https://doi.org/10.1038/s41378-024-00711-7
32 D. Esposito, E. Andreozzi, A. Fratini, G. D. Gargiulo, S. Savino, V. Niola, and P. Bifulco: Sensors **18** (2018) 2553. https://doi.org/10.3390/s18082553
33 G. Ogris, M. Kreil, and P. Lukowicz: Proc. 11th IEEE Int. Symp. Wearable Comput., Boston, USA (IEEE, 2007) 1–4. https://doi.org/10.1109/ISWC.2007.4373776
34 R. Chen, A. Frisoli, and D. Chiaradia: IEEE/ASME Trans. Mechatron. **31** (2025) 1. https://doi.org/10.1109/TMECH.2025.3593667
35 B. Kalita, A. Leonessa, and S. K. Dwivedy: Actuators **11** (2022) 288. https://doi.org/10.3390/act11100288
36 D. R. Higueras-Ruiz, K. Nishikawa, H. Feigenbaum, and M. Shafer: Bioinspir. Biomim. **17** (2022) 011001. https://doi.org/10.1088/1748-3190/ac3adf.
37 C.-P. Chou and B. Hannaford: IEEE Trans. Robot. Autom. **12** (1996) 90. https://doi.org/10.1109/70.481753
38 B. Tondu: J. Intell. Mater. Syst. Struct. **23** (2012) 225. https://doi.org/10.1177/1045389X11435435
39 T. E. Pillsbury, C. S. Kothera, and N. M. Wereley: Bioinspir. Biomim. **10** (2015) 055006. https://doi.org/10.1088/1748-3190/10/5/055006
40 K. P. Ashwin and A. Ghosal: Appl. Mech. Rev. **70** (2018) 040802. https://doi.org/10.1115/1.4041660
41 B. Jamil and Y. Choi: IEEE/ASME Trans. Mechatron. **26** (2021) 3243. https://doi.org/10.1109/TMECH.2021.3056563

About the Authors

Christian Rey M. Alison received his B.S. degree in electronics and communications engineering from the University of Science and Technology of Southern Philippines (USTP) in 2020 and currently is pursuing his M.S. degree in electrical engineering at the same university with a focus on biomedical engineering and instrumentation. From 2024 to the present, he has been serving as a faculty member of the Biomedical Engineering Department of USTP. In 2025, he was one of the delegates to the Taiwan Education Experience Program (TEEP) where he stayed at National Chin Yi University (NCUT) for six months under a research internship.
(christianrey.alison@ustp.edu.ph)

Loryliza D. Bulay-og received her B.S. degree in electronics and communications engineering from Cebu Institute of Technology, Philippines, in 1994, M.S. degree in engineering from Xavier University-Ateneo de Cagayan in 2008, and Ph.D. degree from Mindanao State University-Iligan Institute of Technology (MSU-IIT), Philippines, in 2018. She started as a telecom engineer, and from 1996 to the present, she has been in academia. Currently, she is serving as a professor at USTP. She was also a research fellow in electronics system design at University of Surrey, England in 2019. Her research interests are in mechatronics, biomedical engineering, and sensors. (lory.bulay-og@ustp.edu.ph)

Aaron Raymond See (Member, IEEE) was born in Manila, the Philippines, and received his B.S. degree in electronics and communications engineering from De La Salle University, Manila, the Philippines, in 2006. He obtained his masters and Ph.D. degrees in electrical engineering with a major in biomedical engineering from Southern Taiwan University of Science and Technology in 2010 and 2014, respectively. Subsequently, he did his postdoctoral research in neuroscience at the Brain Research Center, National Tsing Hua University, Hsin Chu, Taiwan. He is currently an associate professor in the Department of Electronic Engineering at National Chin-Yi University of Technology. His research interests are in assistive device development, haptics, and visuotactile sensors. (aaronsee@gm.ncut.edu.tw)